Mon. Not. R. Astron. Soc. **000**, 1–?? (2011) Printed 18 January 2012 (MN LATEX style file v2.2)

Measuring the black hole masses in accreting X-ray binaries by detecting the Doppler orbital motion of their accretion disk wind absorption lines

Shuang-Nan Zhang [1, 2], Jinyuan Liao [1], Yangsen Yao [3⋆]
[1] *Key Laboratory of Particle Astrophysics, Institute of High Energy Physics, Chinese Academy of Sciences, Beijing 100049, China*
[2] *Space Science Division, National Astronomical Observatories of China, Chinese Academy of Sciences, Beijing 100012, China*
[3] *Center for Astrophysics and Space Astronomy, University of Colorado, Boulder, CO 80309, USA*

arXiv:1201.3451v1 [astro-ph.HE] 17 Jan 2012

Accepted date. Received date

ABSTRACT

So far essentially all black hole masses in X-ray binaries have been obtained by observing the companion star's velocity and light curves as functions of the orbital phase. However a major uncertainty is the estimate of the orbital inclination angle of an X-ray binary. Here we suggest to measure the black hole mass in an X-ray binary by measuring directly the black hole's orbital motion, thus obtaining the companion to black hole mass ratio. In this method we assume that accretion disk wind moves with the black hole and thus the black hole's orbital motion can be obtained from the Doppler velocity of the absorption lines produced in the accretion disk wind. We validate this method by analyzing the Chandra/HETG observations of GRO J1655–40, in which the black hole orbital motion ($K_{\rm BH} = 90.8 \pm 11.3$ km s^{-1}) inferred from the Doppler velocity of disk-wind absorption lines is consistent with the prediction from its previously measured system parameters. We thus estimate its black hole mass ($M_{\rm BH} = 5.41^{+0.98}_{-0.57}\ M_\odot$) and then its system inclination ($i = 72.0^{+7.8}_{-7.5}\ ^\circ$), where $M_{\rm BH}$ does not depend on i. Additional observations of this source covering more orbital phases can improve estimates on its system parameters substantially. We then apply the method to the black hole X-ray binary LMC X–3 observed with HST/COS near orbital phase 0.75. We find that the disk-wind absorption lines of C IV doublet were shifted to $\sim$ 50 km s^{-1}, which yields a companion-to-black-hole mass ratio of 0.6 for an assumed disk wind velocity of -400 km s^{-1}. Additional observations covering other orbital phases (0.25 in particular) are crucial to ease this assumption and then to directly constrain the mass ratio. This method in principle can also be applied to any accreting compact objects with detectable accretion disk wind absorption line features.

1 INTRODUCTION

Black holes (BHs) are believed to exist in many X-ray binaries (XRBs) and active galactic nuclei (AGN). Measurement of the motion of a BH with respect to its surrounding in such a system can in principle set strong constraints on the mass of the BH. However in an AGN this is normally not possible because the time scale of BH's significant motion is too long and/or the BH is barely moving at all. In an XRB, the BH should move with respect to the system's center of mass (CM), making it possible to detect directly the BH's motion with respect to the CM. However in a low-mass XRB (LMXB) the companion is normally much less massive than the BH, so that the BH barely moves or moves very slowly with respect to the CM. In some LMXBs, the companion's mass is comparable or only several times less massive than the BH, e.g., in GRO J1655–40 (Zhang et al. 1994; Orosz & Bailyn 1997), the BHs' motion may be significant enough for direct detection. The most favorable systems for detecting BH's motion should be high-mass XRBs (HMXBs), in which the BHs move rapidly with respect to their CMs.

Orbital motion of double-peaked disk emission lines were observed for neutron star XRB Sco X–1 (Steeghs & Casares 2002), the BH XRB A0620–00 (Haswell & Shafter 1990; Orosz et al. 1994), and the BH GRS 1124–68 (Orosz et al. 1994). Unfortunately a significant phase offset of velocity modulation was found from that expected based on the observed orbital motion of the companion, though the velocity semi-amplitude is consistent with the expected mass ratio (Orosz et al. 1994). Soria et al. (1998) observed the orbital motion of the double-peaked disk emission line He II λ4686 from GRO J1655–40, and found its velocity modulation phase and semi-amplitude in agreement with the kinematic and dynamical parameters of the system. Therefore a more robust mass lower limit is placed

based on the observed motion of the primary and thus ruling out any possibility for a neutron star as the primary in the system (Soria et al. 1998). However one major problem in accurately measuring the orbital motion of the primary from the observed double-peaked emission lines is how to determine reliably the line center, because the lines are typically asymmetric and also variable.

In an XRB, both the accretion disk and its wind move with the BH, and thus provides us with another opportunity to measure the BH's motion via Doppler shift of absorption features of the accretion disk wind. Accretion disk winds are ubiquitous in XRBs and normally detected through ionized absorption lines, typically with around $\sim 10^3$km s^{-1} or less (e.g., Ueda et al. 2004; Miller et al. 2004, 2006, 2008), but can reach to about $\sim 10^4$km s^{-1} in some extreme cases, e.g. in the newly discovered BH transient IGR J17091–3624 (King et al. 2011). In particular the high quality Chandra/HETG observations of the BHXB GRO J1655–40 have found many highly ionized narrow absorption lines, which are interpreted as evidence of magnetic field-driven accretion disk wind (Miller et al. 2006; Kallman et al. 2009; Luketic et al. 2010); although the absorption lines are also interpreted as from the absorption by X-ray heated thermal wind (Netzer 2006). Regardless the origin of the accretion disk wind, the orbital motion of its many absorption lines may be measured reliably, because typically many narrow absorption lines are present with high signal to noise ratios and appear to be rather stable when observed.

In this work, we model the Doppler motion of wind absorption lines from the LMXB GRO J1655–40 and HMXB LMC X–3 to constrain directly the companion to primary mass ratio, in order to measure their BH masses and orbital inclination angles. We first describe the methodology and test its feasibility by applying it to Chandra/HETG observations of GRO J1655–40, revealing for the first time the velocity modulation of wind absorption lines in an XRB and thus providing a new measurement of its BH motion and orbital inclination angle. We then apply this method to the HST/COS observations of LMC X–3 attempting to constrain the companion to primary mass ratio. Finally we discuss further observations needed to achieve the required accuracy of BH mass estimate for LMC X–3, as well as potential problems and uncertainties of applying this method.

2 METHODOLOGY

So far, all BH masses in XRBs have been estimated using the Kepler's 3rd law of stellar motion, expressed in the so called the mass function,

$$f(M) \equiv P_{\rm orb}K_{\rm C}^3/2\pi G = M_{\rm BH}\sin^3 i/(1+q)^2, \qquad (1)$$

where $P_{\rm orb}$ is the orbital period, $K_{\rm C}$ is the semi–amplitude of the velocity curve of the companion star, $M_{\rm BH}$ is BH mass, i is the the orbital inclination angle, and $q \equiv M_{\rm C}/M_{\rm BH}$ is the mass ratio. Since the only direct observables are $P_{\rm orb}$ and $K_{\rm C}$, both $M_{\rm C}$ and i have to be determined indirectly in order to obtain the BH mass estimate reliably. The companion's mass $M_{\rm C}$ can be determined relatively reliably by the observed spectral type of the companion star. For LMXBs, i can be estimated by modeling the optical or infrared light curve modulation, though model dependence and other uncertainties (such as accretion disk contamination) cannot be circumvented completely. For HXMBs, i is normally not determined very well; in many cases observations or lack of eclipse of the accretion disk emission by the companion is used to put some constraints on the possible ranges of i. For details of BH mass estimates using this method, please refer to Remillard & McClintock (2006).

On the other hand, the mass ratio q can be determined directly according to the law of momentum conservation, i.e.,

$$M_{\rm C}/M_{\rm BH} = K_{\rm BH}/K_{\rm C}, \qquad (2)$$

if the semi–amplitude of the velocity curve of the BH $K_{\rm BH}$ can be observed directly. Since a BH is not directly observable, we can only hope to observe any emission or absorption line feature co-moving with it. The accretion disk certainly moves with the accreting BH. However any line feature of the inner accretion disk suffers from the broadening of disk's orbital motion and distortions by relativistic effects around the BH, thus making it practically impossible, or difficult to the least, for detecting the binary orbital motion of the BH. Emission line features from the outer disk region are normally detected with double-peaks, which can be modeled to obtain the semi–amplitude of the velocity of the compact object, as discussed above. However a major uncertainty is to determine the mean separation between the emission regions of the blue-shifted and red-shifted components.

Fortunately, as we have discussed above, absorption line features of accretion disk winds in BHXBs have been routinely detected with high significance. This suggests that the accretion disk wind in an XRB moves with the disk that produces the wind, since otherwise the wind from the disk would not intercept the continuum emissions produced from the same disk. In this case, the Doppler motion of wind absorption line features can be considered as that of the BH, unless the wind interacts strongly with the surrounding interstellar medium or the wind intrinsic velocity has systematic orbital dependence. It has been found recently that large scale (pc) cavities exist around microquasars (XRBs producing relativistic jets), and perhaps are ubiquitous in all BHXBs producing strong winds (Hao & Zhang 2009). This suggests that at least in the vicinity of the BH the wind cannot interact directly with interstellar medium. The interactions of disk winds with interstellar medium at pc scale would not complicate the observations, because it takes much longer than an orbital period before the winds could arrive at the boundaries of these cavities, and thus the wind should have lost any possible memories of the orbital motion of the compact object. For disk-fed accretion, the wind velocity is not expected to have any orbital phase modulation; for stellar-wind accretion the focused wind may complicate the situation considerably though. We therefore suggest to apply this method to only those systems in which the accretion is disk-fed, i.e., no significant wind interaction happens between the stellar and accretion disk winds. Nevertheless only observations can tell us in which kinds of systems this method can be used reliably.

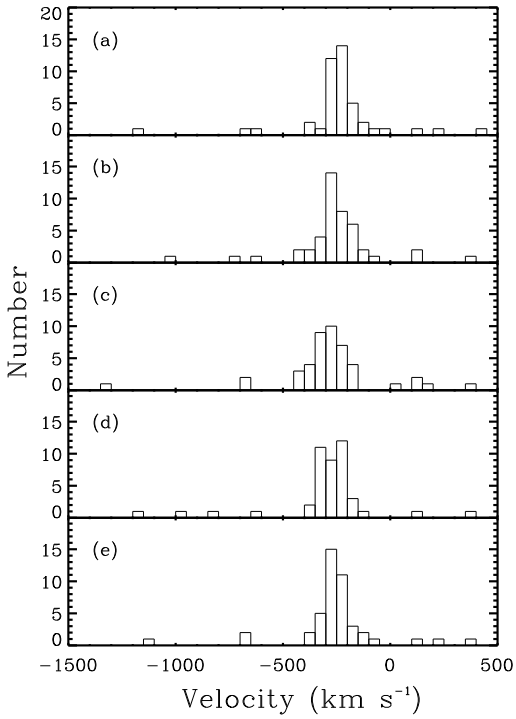


Figure 1. Distributions of the line velocities in four equally spaced intervals and their average values, during the Chandra/HETG observations lasting for more than 60 ksec; note that here the system velocity of the BH XRB has already been subtracted. Panels from (a) to (d) corresponding to the phases shown in Fig. 2 from left to right.

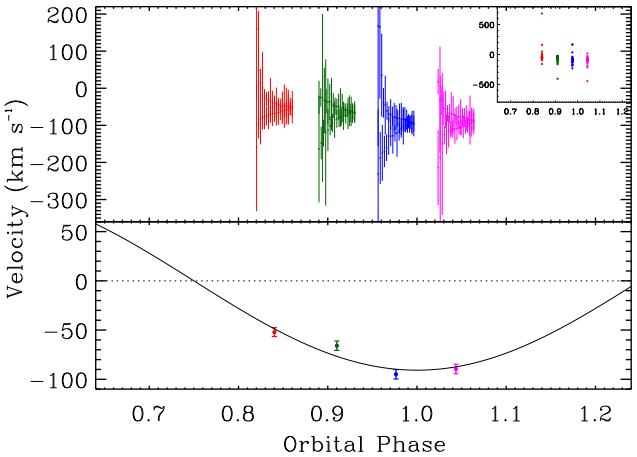


Figure 2. Velocity curve of the 39 observed absorption lines, after rejecting six lines as suspected outliers and subtracting the line of sight intrinsic velocity of each line at each orbital phase. The upper panel marks the velocity of each line with its 1-σ error bar slightly shifted horizontally for visual clarity; the inset shows all velocities, including the three data points out of the range in the main panel. The bottom panel shows the weighted average velocity of all lines in the upper panel at each phase; the solid curve is the fitted velocity curve with its orbital period and phase fixed at the values observed previously.

3 APPLICATION TO THE LMXB GRO J1655–40: A TEST STUDY

GRO J1655–40, discovered as an X-ray transient by Zhang et al. (1994), is a well-known and best studied BHXB and the second source with superluminal relativistic jets detected (Tingay et al. 1995; Harmon et al. 1995; Hjellming & Rupen 1995). Its system parameters remain so far the best measured among all known BHXBs, with $P_{\rm orb} = 2.62191 \pm 0.00020$ d, $1/q \equiv M_{\rm BH}/M_{\rm C} = 2.6 \pm 0.3$, $i = 70.2 \pm 1.9^\circ$, and $M_{\rm BH} = 6.3 \pm 0.5\ M_\odot$ (all 95% confidence) (Orosz & Bailyn 1997; Greene et al. 2001). Its precise BH mass and inclination measurements allow its BH spin parameter determined from its X-ray continuum fitting, first proposed by Zhang et al. (1997) and then refined by incorporating detailed modeling of various effects (e.g., Yao et al. 2005; Li et al. 2005; Davis et al. 2005; Shafee et al. 2006; Steiner et al. 2009; McClintock et al. 2011). However possible sources of systematic errors are in the modeling of the ellipsoidal light modulation of the companion star and contamination of the disk's continuum emission in the optical to infrared bands. Soria et al. (1998) observed the velocity curve of the double-peaked disk emission line He II λ4686 from GRO J1655–40, and derived its projected radial velocity semi-amplitude determined for the primary as $K_{\rm BH} = 76.2 \pm 7.5$ km s^{-1}, yielding $M_{\rm BH} = 6.62 \pm 0.74\ M_\odot$ and $i = 66.6 \pm 7.7^\circ$ (all 68.3% confidence), fully consistent with that determined from the companion's velocity curve and ellipsoidal light variation.

Miller et al. (2006) detected many narrow and ionized absorption lines with High Energy Transmission Grating (HETG) Chandra observations of GRO J1655–40. The exact position of the point source cannot be determined accurately in the zeroth order image, which is severely piled-up due to its high flux. An offset in the source position will cause a systematic shift of all lines in the wavelength space. However, this shift is mostly canceled out in the combined total spectrum if each line is detected in the spectra of both the $+1$ and -1 orders with similar count spectra. However the combined lines will be broadened by the unknown systematic offset, which in turn will cause larger uncertainties in determining the center of each line. There may also exist other sources of systematic errors which can cause offset between the centers of the same line in the spectra of the $+1$ and -1 orders.

Here we determine the position of the zeroth order image by minimizing the relative offsets between the absorption lines in the $+1$ and -1 orders, and estimate the systematic error in determining the center wavelength of each absorption line. We first fit each absorption line feature with a Gaussian profile in the $+1$ and -1 orders of the High Energy Grating (HEG) and Medium Energy Grating (MEG) separately, i.e., we get a pair of profiles for each absorption line, integrated over the whole observation in order to get the highest signal to noise ratio. The local continuum around each line is assumed to have a power-law shape, but our results are insensitive to the continuum shape. For HEG and MEG we obtain 43 and 9 pairs of absorption lines with at least 3-σ detection, resulting in 43 and 9 differences of the central wavelengths of these pairs, respectively. We then use the Bayesian method to find the offset d and its systematic

error $\sigma_{\rm s}$ by maximizing the following function,

$$p(d,\sigma_{\rm s}) = \frac{1}{\sqrt{(2\pi)^n}} \prod \frac{1}{\sqrt{{\sigma_{x_k}}^2+\sigma_{\rm s}^2}} e^{-\frac{(d-x_k)^2}{2({\sigma_{x_k}}^2+\sigma_{\rm s}^2)}}, \quad (3)$$

where x_k and σ_{x_k} are the wavelength difference and its statistical error of the k-th pair ($k = 1$ to n, and $n = 43$ for HEG or 9 for MEG), respectively. Finally for HEG we get $d = (4.8 \pm 0.1) \times 10^{-3}$ Å and $\sigma_{\rm s} = (3.2 \pm 1.3) \times 10^{-4}$ Å.

We thus take the error for d as $\sigma_d = \sigma_{\rm s} = 3.2 \times 10^{-4}$ Å for HEG. Similarly for MEG we get $d = (9.7 \pm 0.8) \times 10^{-3}$ Å for MEG, where $\sigma_d = 9 \times 10^{-4}$ Å is dominated by the systematic error. Taking these additional errors for MEG and HEG line wavelengths and requiring all pairs in HEG with $d = 4.8 \times 10^{-3}$ Å and in MEG $d = 9.7 \times 10^{-3}$ Å, we have a total $\chi^2 = 55$ for 50 degrees of freedom, thus validating our method of determining the systematic errors. Since the wavelength bin (an image pixel) is 2.5×10^{-3} Å or 5.0×10^{-3} Å for HEG or MEG, we thus shift the spectra of the -1 and the $+1$ orders by one bin, towards the decreasing (-1 order) and increasing ($+1$ order) wavelength directions, respectively. This is identical to shifting the location of the point source by one pixel in the zeroth order image. Finally we combine the two shifted spectra as one single spectrum.

Because the observations lasted for about a quarter of the orbital phase of GRO J1655–40 and many absorption lines have high signal to noise ratios, here we divide the observations into four equal orbital internals in order to detect the orbital motion of the absorption lines. For each combined spectrum we again fit each absorption feature with a Gaussian profile to determine its central wavelength, line width and intensity. Table 1 lists the 45 lines in all four intervals with at least 3-σ detection that are included for further analysis; here only statistical errors are shown.

Fig. 1 shows the velocity distributions of the four groups of 45 lines and their average velocities; note that here the system velocity of the BH XRB has already been subtracted. Adopting the orbital period and phase ephemeras from Greene et al. (2001) and assuming that the BH's motion is exactly anti-phased with the companion's motion (Soria et al. 1998), we fit velocities of these lines simultaneously to a sinusoidal function. In the fit, the intrinsic velocity of each line is a free parameter, but all lines in the same orbital phase follow the same orbital modulation. This way we have 46 free parameters (45 intrinsic velocities for all these lines plus the line of sight velocity amplitude of the black hole) with 180 data points. The fit results in $K_{\rm BH} = 93.8 \pm 11.1$ km s^{-1} with $\chi^2 = 179$ for 134 degrees of freedom; the systematic errors determined above are included for all lines.

Considering that some lines may be outliers, we reject the four groups of six lines with central velocities more than 300 km s^{-1} from the median values of each distribution, as listed in Table 1. The remaining four groups of 39 lines have velocity dispersion (1-σ) of about 60 km s^{-1}, i.e., the rejected lines are more than 5-σ away from the median values. The fit to the remaining four groups of 39 lines yields $K_{\rm BH} = 90.8 \pm 11.3$ km s^{-1} with $\chi^2 = 131$ for 116 degrees of freedom, a marginal improvement over the full dataset fit. This means that the deviations of these possible outliers are not significant statistically and thus do not deserve further studies at this stage. Fig. 2 shows the fitting results; please note that the velocities are obtained by subtracting the fitted line of sight intrinsic velocity of each line from the obtained central velocity of each line at this orbital phase. It is worth noting that the phase zero in this system was defined as that when the companion is receding from the observer at the maximum velocity (Orosz & Bailyn 1997). Nevertheless both results are statistically consistent with $K_{\rm BH} = 76.2 \pm 7.5$ km s^{-1} obtained by Soria et al. (1998). If we fit the four groups of 39 lines to a straight line, we get $\chi^2 = 813$ for 154 degrees of freedom. The linear model is thus rejected with high significance, compared to the sinusoidal model.

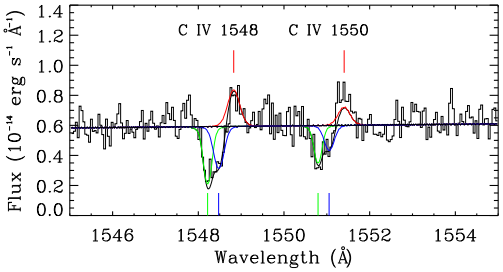


Figure 3. Spectrum of the available HST/COS observations around C IV doublet. Red curves indicate the fit to the emission from the heated surface of the companion star, green curves are the fit to the Galactic ISM absorptions at 0 km s^{-1} , and blue curves indicate the fit to the accretion disk wind absorptions at $\approx$ 50 km s^{-1} (local velocity ≈ -400 km s^{-1}). The vertical bars mark the central positions of these components.

With the fitted $K_{\rm BH} = 90.8 \pm 11.3$ km s^{-1} and taking the other system parameters (except the inclination) of GRO J1655–40 from Greene et al. (2001), we first obtain its BH mass $M_{\rm BH} = 5.41^{+0.98}_{-0.57}$ $M_\odot$ from Eq. 2 and then its system inclination $i = 72.0^{+7.8}_{-7.5}$ ° from Eq. 1, respectively. All these (1-σ) errors are obtained by Monte-Carlo samplings, because of the asymmetry and coupling of some errors. These parameters, albeit with large uncertainties due to the very incomplete orbital coverage of observations, are consistent with all previous measurements. Therefore the existing data of GRO J1655–40 validate our proposal that absorption lines produced in the accretion disk wind can be used to measure directly the orbital motion of the BHs in BHXBs.

4 APPLICATION TO THE HMXB LMC X–3

LMC X–3 is another excellent object for applying this method. It is a bright XRB system in the Large Magellanic Cloud composed of a B3 V star and a central BH, and receding away from us at a systemic velocity $V_{\rm S} = +310$ km s^{-1} (Cowley et al. 1983; hereafter C83). It is one of the few BH systems that are persistently luminous in both X-ray and far-ultraviolet (FUV) wavelength bands. The BH is believed to be undergoing accretion from its B-star companion via Roche lobe overflow with an orbital period of 1.7 days (C83); we therefore do not expect any significant contamination of the stellar wind to any absorption features of its accretion disk wind. Spectroscopic observations of

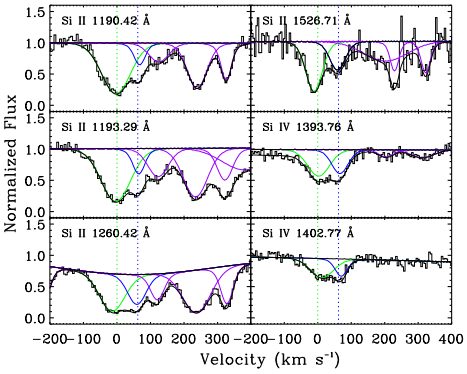


Figure 4. Si II and Si IV absorption features in the spectrum of the previous HST/COS G130M observations, normalized to the continuum flux. The apparent higher velocity components (marked with pink curves) may be produced in the outer part of the disk wind at lower local velocities.

the B star indicate a large radial velocity semi-amplitude, $K_{\rm C} = 235 \pm 11$ km s^{-1} (C83). Taken the mass of the B3 V star as about 6 $M_{\odot}$, the BH mass in LMC X–3 is thus estimated to be $5 - 10$ $M_{\odot}$, assuming an inclination angle of $50^{\circ} - 70^{\circ}$ (C83; Kuiper et al. 1988; Soria et al. 2001). Because of the considerable uncertainty in its inclination (and thus BH mass), its BH spin has not been reliably determined yet with the X-ray continuum modeling method (e.g., Zhang et al. 1997; Steiner et al. 2010). Since the BH should be moving at a comparable velocity to its companion, it is possible to directly measure its orbital motion if the absorption lines produced in its accretion disk wind are detected.

Although LMC X–3 has been intensively studied in the X-ray band, the previously operated and currently operating X-ray spectroscopic instruments lack the combination of the required sensitivity and resolution to measure the expected Doppler motion of any accretion wind absorption features. High resolution UV spectroscopic observations of this source are rather sparse; so far only two *FUSE* observations and four observations with the Cosmic Origins Spectrograph (COS) onboard the *Hubble Space Telescope* (HST) (HST/COS hereafter) to LMC X–3 have been made (Hutchings et al. 2003; Wang et al. 2005; Song et al. 2010, here after S10). Again *FUSE* does not have the combination of the required sensitivity and the observations did not produce spectra with high enough signal to noise ratio for the purpose of this investigation. The HST/COS does have the required performance to do so, although the available observations only covered a small portion of the orbital period of LMC X–3. In this work, we analyze the available HST/COS UV spectroscopic observations of LMC X–3, aiming at constraining the systemic parameters and further demonstrating the feasibility of our proposed new method of measuring the BH's mass in an XRB.

From the *FUSE* and HST/COS observations, S10 detected variable O VI and N V emission lines and found that variability of their intensities are inconsistent with expectation of a stellar wind origin. So they attributed them to the heated stellar surface of the companion star. In fact both absorption and emission features are detected in N V (with G130M) and C IV (with G160M) doublets (Fig. 2 in S10) in the HST/COS observations (Program 11642; please refer to S10 for detailed description of the HST/COS observations and data analysis). However, since S10 focused on the origin of the emission variability and the connection between the emission features and the systemic parameters, these absorption features have not been explored in detail.

Here we analyze the C IV doublet complexes (we do not conduct the same analysis to the N V features because the absorptions are much less significant than those of C IV). In Fig. 3, we decompose the observed C IV doublet into three components for each line: one emission component and two absorption components. The emission component is assumed to come from the heated surface of the companion, the same as the O VI and N V emission lines (S10); its width and Doppler shift are fixed to those inferred from the O VI and N V emission lines in the decomposition. One absorption component (at zero velocity) is assumed to come from the Galactic ISM absorption. The other significant absorption component has a redshift of about 50 km s^{-1}, and may have two possible origins. One is the absorption produced in the stellar wind of the B3 V companion star. However, the orbital phase of the binary system was about 0.75 during the HST/COS observations, i.e., the straight line connecting the companion star and the BH is perpendicular to our LOS (please be noted that, in contrast to GRO J1655–40, the orbital phase zero in LMC X–3 was defined as that when the BH is at its superior conjunction, i.e., the companion is just between the observer and the BH; Cowley 1983; S10). In order for any stellar wind to intercept significantly the emission from the inner disk region, a significant amount of stellar wind has to stream to the inner disk region, i.e., the system must be wind-fed, against the common believe that LMC X–3 is actually disk-fed. We thus rule out this possibility. The other and the only viable scenario is the absorption by the accretion disk wind, making it possible to directly measure the orbital motion of the BH. It is worth noting that the measured C IV column density in the ISM [$\log N_{\rm ISM}({\rm cm}^{-2}) = 13.7 \pm 0.1$] agrees remarkably well with predicted value [$\log N_{\rm CIV}({\rm cm}^{-2}) = 13.8$] in a joint analysis of the X-ray and FUV spectroscopic observations of LMC X–3 (Yao et al. 2009), indirectly validating such a component decomposition.

With the measured velocity $V_{0.75} = 51.3 \pm 4.1$ km s^{-1} of C IV absorption lines tracing the BH motion and considering the systemic velocity ($V_{\rm S} = +310$ km s^{-1}) of LMC X–3 and velocity semi-amplitude of the companion star $K_{\rm C} = 235$ km s^{-1}, we can constrain the companion to black hole mass ratio. At phase 0.75, the BH is receding from us at the maximum speed, and thus the relation of $V_{0.75}$ and $K_{\rm BH}$ can be expressed as

$$V_{0.75} = V_{\rm wind} + V_{\rm S} + K_{\rm BH}, \qquad (4)$$

where $V_{\rm wind}$ is the intrisinc velocity of the accretion disk wind in our LOS. Assuming $V_{\rm wind} = -400$ km s^{-1}, a similar wind velocity found in GRO J1655–40 (Miller et al. 2006), from Eq. 4 we obtain $K_{\rm BH} \sim 140$ km s^{-1}. Plugging these numbers in Eq. 2, we further obtain $q = M_C/M_{\rm BH} \sim 0.6$, which is consistent with the ratio usually adopted for the LMC X–3 system (e.g., C83). We therefore suggest that the observed C IV absorption feature is consistent to our model that the accretion disk wind moves with the BH and the observed Doppler shift is a combination of the wind velocity and the BH's orbital velocity in our LOS.

In the above exercise, we assumed a $V_{\rm wind}$ in order to obtain $K_{\rm BH}$, since there is a degeneracy of $V_{\rm wind}$ and $K_{\rm BH}$ in Eq. 4. Unfortunately, the HST/COS G160M observation analyzed above only lasted for one HST orbit, and thus cannot break the degeneracy, i.e., we cannot put an independent measure of the BH's velocity, without observing the orbital modulation of the Doppler motion of the wind. The HST/COS G130M observations in a shorter wavelength band covered a much larger part of the orbital period. As shown in Fig. 4, the combined spectrum revealed several complicated absorption features. Nevertheless, Si II and Si IV absorption lines at $V_{0.75} \approx 50$ km s^{-1} are also detected; the apparent higher velocity components may arise from the outer part of the accretion disk with lower local velocities, mimicking the different velocities and ionization zones of AGN warm-absorbers/outflows (e.g., Arav et al. 2005). However, the combination of the complexity of the observed absorption features and the rather incomplete orbital phase coverage of these previous HST/COS observations does not warrant further more quantitative analysis for breaking the above mentioned degeneracy and probing the nature of those higher velocity components.

Clearly, observations covering more orbital phases are badly needed to break the degeneracy. Observations around phase 0.25 are the most favorable ones for this purpose. In contrast to the existing observations taken around 0.75 in which the BH is receding at the maximum velocity from us, at phase 0.25, the BH is expected to be moving toward us at the maximum velocity, so is the disk wind. Therefore, the relation between $V_{0.25}$ and $K_{\rm BH}$ can be expressed as

$$V_{0.25} = V_{\rm wind} + V_{\rm S} - K_{\rm BH}. \quad (5)$$

If $V_{\rm S} = -400$ km s^{-1} as assumed, the $V_{0.25}$ is expected to be at -230 km s^{-1}. The real measurement of $V_{0.25}$ from the future observations, together with $V_{0.75}$ measured from the existing observations, would allow us to solve $V_{\rm wind}$ and $K_{\rm BH}$ from Eqs. 4 and 5 and then to reliably constrain $M_C/M_{\rm BH}$ and system inclination angle i (Eqs. 2 and 1).

5 SUMMARY AND DISCUSSION

As shown in Eq. 2, $M_{\rm BH}$ can be directly obtained if $K_{\rm BH}$ can be measured, in addition to $M_{\rm C}$ and $K_{\rm C}$ measured by observing the companion star. In this work we suggest to measure $K_{\rm BH}$ by detecting the Doppler orbital motion of the accretion disk wind absorption lines, assuming that the accretion disk wind moves with the BH and does not have systematic orbital phase dependence. This method has the potential of circumventing the model dependence and other uncertainties in estimating the orbital inclination angle, that is required in the method commonly used to measure the BH masses in XRBs by detecting the companion star's velocity and light curves, as shown in Eq. 1. Actually knowing the mass ratio with Eq. 2, one can in turn use Eq. 1 to derive the inclination angle, which can be used to calibrate the light curve model used previously to derive the inclination angle.

Our analysis of the previous Chandra/HETG observations of GRO J1655–40 have revealed wind velocity modulation consistent with the orbital motion of the BH predicted from its previously measured system parameters. An independent projected radial velocity semi-amplitude measured here allows its inclination angle determined without using the modeling of its ellipsoidal light modulation of its companion. We find its BH radial velocity semi-amplitude $K_{\rm BH} = 90.8 \pm 11.3$ km s^{-1}, BH mass $M_{\rm BH} = 5.41^{+0.98}_{-0.57}\ M_\odot$ and system inclination $i = 72.0^{+7.8}_{-7.5}\ ^\circ$, where $M_{\rm BH}$ does not depend on i at all. However the very limited orbital coverage of the observations does not allow more accurate system parameter measurements of this binary system. Nevertheless with the velocity component of its orbital motion removed, we can obtain more accurate measurements of the intrinsic velocities of each line along our line of sight, and thus may be able to constrain further the physical properties of the wind, by combining with the velocity broadenings of these lines; this is the subject our future work.

Our analysis of the previous HST/COS observations of the HMXB LMC X–3 has found absorption line features consistent with that predicted by assuming the previously measured dynamical parameters of LMC X–3 and the wind properties in LMC X–3 being similar to that observed in another BHXB GRO J1655–40. Given the limitations of the previous HST/COS observations of LMC X–3 that do not allow to break the degeneracy of the wind velocity and the BH orbital velocity, new HST/COS observations are required to cover significantly different orbital phases.

As mentioned in S10, the C IV features shown in Fig. 3 might be P-cygni profiles. However, the emission features agree well with all other emission lines detected, which are attributed to the heated stellar surface. Therefore it is more reasonable to attribute the emission features in Fig. 3 to the heated stellar surface (as done in S10), thus invalidating the P-cygni profile interpretation. UV emission lines produced from the heated stellar surface are not unique in the system of LMC X–3, but rather a common feature observed in XRBs (e.g., Vrtilek et al. 2003). Of course new observations suggested above would definitely reveal the nature of the the C IV features shown in Fig. 3.

In this work, we have also assumed that the accretion disk wind velocity is constant, at least during one full orbital phase, in order to apply this method reliably. In reality, the intrinsic wind velocity may have random fluctuations, though the fluctuations do not seem to be significant in GRO J1655–40 (Miller et al. 2006). However, it has been known that wind absorption features are not always detected and it is also not fully understood when and why wind absorptions are present or absent. Future high signal to noise observations covering more orbital phases may shed some lights on this problem and test ultimately if our suggested method can be applied reliably and produce accurate BH mass measurements in BHXBs. The joint JAXA/NASA *ASTRO-H* mission is particularly suitable for making such observations, with its high-throughput spectroscopy provided by the micro-calorimeter with high spectral resolution of $\Delta E \sim 7$ eV (Takahashi et al. 2010). Finally we should point out that this method in principle can also be applied to other accreting compact objects, such accreting neutron star and white dwarf binaries, with detectable accretion disk wind absorption line features.

ACKNOWLEDGMENTS

S.N.Z. thanks the hospitality of CASA, University of Colorado at Boulder, during his visit in December 2010 when the initial idea of this work emerged as results of some interesting discussions with local scientists there. The anonymous referee is thanked for making several useful comments and suggestions. We appreciate comments and suggestions made by Drs. Zhongxiang Wang and Hua Feng. Daniel Dewey is thanked for his information and suggestion on evaluating the systematic errors. S.N.Z. also acknowledges partial funding support by the National Natural Science Foundation of China under grant nos. 11133002, 10821061, 10725313, and by 973 Program of China under grant 2009CB824800. Y.Y. appreciates financial support by NASA through grant HST-GO-11642.01-A.

REFERENCES

Arav, N., et al. 2005, ApJ, 620, 665
Boyd, P. T., et al. 2001, 555, 822
Begelman, M. C., et al. 1983, ApJ, 271, 70
Cowley, A. P., et al. 1983, ApJ, 272, 118 (C83)
Cowley, A. P., et al. 1994, ApJ, 429, 826
Davis, S. W., Blaes, O. M., Hubeny, I., & Turner, N. J. 2005, ApJ, 621, 372
Greene, J., Bailyn, C. D., & Orosz, J. A. 2001, ApJ, 554, 1290
Hao, J. F., & Zhang, S. N. 2009, ApJ, 702, 1648
Harmon, B. A., Wilson, C. A., Zhang, S. N., et al. 1995, Nature, 374, 703
Haswell, C. A., & Shafter, A. W. 1990, ApJ, 359, L47
Hjellming, R. M., & Rupen, M. P. 1995, Nature, 375, 464
Hutchings, J. B., et al. 2003, AJ, 126, 2368
Kallman T. R., Bautista M. A., Goriely S., Mendoza C., Miller J. M., Palmeri P., Quinet P., Raymond J., 2009, ApJ, 701, 865
King A. L., et al., 2012, ApJL, in press, arXiv:1112.3648
Kuiper, L., et al. 1988, A&A, 203, 79
Li, L.-X., Zimmerman, E. R., Narayan, R., & McClintock, J. E. 2005, ApJS, 157, 335
Luketic, S., et al. 2010, ApJ, 719, 515
McClintock, J. E., Narayan, R., Davis, S. W., et al. 2011, Classical and Quantum Gravity, 28, 114009
Miller, J. M., et al. 2004, ApJ, 601, 450
Miller, J. M., et al. 2006, Nature, 441, 953
Miller, J. M., et al. 2008, ApJ, 680, 1359
Netzer, H. 2006, ApJ, 652, L117
Orosz, J. A., Bailyn, C. D., Remillard, R. A., McClintock, J. E., & Foltz, C. B. 1994, ApJ, 436, 848
Orosz, J. A., & Bailyn, C. D. 1997, ApJ, 477, 876
Remillard, R. A., & McClintock, J. E. 2006, ARA&A, 44, 49
Shafee, R., McClintock, J. E., Narayan, R., et al. 2006, ApJ, 636, L113
Song, L., et al. 2010, AJ, 140, 794
Soria, R., Wickramasinghe, D. T., Hunstead, R. W., & Wu, K. 1998, ApJ, 495, L95
Soria R., et al. 2001, A&A, 365, L273
Steeghs, D., & Casares, J. 2002 ApJ, 1, 273
Steiner, J. F., McClintock, J. E., Remillard, R. A., Narayan, R., & Gou, L. 2009, ApJ, 701, L83
Steiner, J. F., et al. 2010, ApJ, 718, L117
Takahashi, T., Mitsuda, K., Kelley, R., et al. 2010, SPIE, 7732, 77320Z
Tingay, S. J., Jauncey, D. L., Preston, R. A., et al. 1995, Nature, 374, 141
Ueda, Y., et al. 2004, ApJ, 609, 325
Vrtilek, S. D., et al. 2003, PASP, 115, 1124
Wang, Q. D., et al. 2005, ApJ, 635, 386
Yao, Y., Zhang, S. N., Zhang, X., Feng, Y., & Robinson, C. R. 2005, ApJ, 619, 446
Yao, Y., et al. 2009, ApJ, 690, 143
Zhang, S. N., Harmon, B. A., Paciesas, W. S., Wilson, C. A., & Fishman, G. J. 1994, IAUC, 6106, 1
Zhang, S. N., et al. 1997, ApJ, 482, L155

Table 1. Velocity and width of each absorption line at each orbital phase, detected with more than 3-σ significance. For each orbital phase, the numbers in the left and right are the velocity shift and width (broadening) of the absorption line; the 1-σ errors are included in the parenthesis. The last column indicates if the line is within 300 km s^{-1} to the median velocity at each phase.

Ion and transition	Wavelength (Å)	Phase 1 (km s^{-1})	Phase 2 (km s^{-1})	Phase 3 (km s^{-1})	Phase 4 (km s^{-1})	Within 300 (km s^{-1})
Ni XXVI $1s^22s-1s^25p$	6.1200	−802(48) 102(88)	−756(50) 115(106)	−821(61) 152(90)	−1338(94) 648(86)	*N*
Ni XXVI $1s^22s-1s^24p$	6.8163	−535(33) 380(39)	−560(29) 329(33)	−478(34) 355(42)	−471(33) 355(38)	*Y*
Ni XXVI $1s^22s-1s^23p$	9.0610	−416(12) 212(15)	−431(15) 241(20)	−453(14) 215(18)	−431(14) 220(18)	*Y*
Ni XXVI $1s^22s-1s^23p$	9.1050	−432(16) 168(21)	−432(13) 134(22)	−465(16) 182(23)	−445(18) 179(26)	*Y*
Fe XXVI $1s-2p$	1.7798	−1339(196) 861(239)	−1187(246) 773(261)	−1473(185) 962(207)	−1107(141) 825(154)	*N*
Fe XXV $1s^2-1s2p$	1.8504	74(142) 1408(157)	−38(117) 1167(131)	−11(120) 2070(135)	368(155) 1436(173)	*N*
Fe XXIV $1s^22s-1s^29p$	6.3475	262(47) 289(57)	250(38) 258(60)	254(30) 103(91)	253(30) 145(52)	*N*
Fe XXIV $1s^22s-1s^26p$	6.7870	−413(11) 155(17)	−410(14) 190(18)	−425(11) 145(18)	−426(12) 154(19)	*Y*
Fe XXIV $1s^22s-1s^25p$	7.1690	−409(7) 261(9)	−412(8) 255(9)	−442(8) 244(9)	−452(9) 280(10)	*Y*
Fe XXIV $1s^22s-1s^24p$	7.9893	−344(8) 353(9)	−357(9) 345(10)	−390(9) 319(10)	−405(8) 321(9)	*Y*
Fe XXIV $1s^22s-1s^23p$	10.6190	−385(16) 295(21)	−393(18) 318(23)	−454(18) 286(23)	−454(20) 335(23)	*Y*
Fe XXIV $1s^22s-1s^23p$	10.6630	−358(19) 328(26)	−388(19) 301(23)	−404(19) 317(24)	−386(19) 308(23)	*Y*
Fe XXIII $2s^2-2s5p$	7.4722	−337(16) 243(23)	−351(16) 247(23)	−330(16) 199(22)	−359(16) 105(30)	*Y*
Fe XXIII $2s^2-2s4p$	8.3029	−204(13) 273(15)	−224(14) 291(17)	−296(14) 261(16)	−280(15) 246(16)	*Y*
Fe XXIII $2s^2-2s3p$	10.9810	−379(16) 178(24)	−387(24) 257(33)	−398(17) 176(27)	−390(16) 116(31)	*Y*
Fe XXIII $2s^2-2s3p$	11.0180	−333(18) 150(29)	−315(19) 164(30)	−360(19) 168(30)	−355(19) 189(25)	*Y*
Fe XXII $2s^22p-2s^23d$	11.7700	−307(33) 147(54)	−324(31) 112(67)	−327(29) 95(51)	−372(32) 127(61)	*Y*
Fe XXII $2s^22p-2s^23d$	11.9200	−286(50) 141(80)	−281(62) 173(103)	−358(56) 208(68)	−324(57) 196(81)	*Y*
Mn XXIV $1s^2-1s2p$	2.0062	509(444) 1259(437)	−582(261) 1018(322)	−7(302) 719(572)	−326(184) 294(359)	*Y*
Cr XXIV $1s-2p$	2.0901	−303(156) 644(271)	−262(180) 531(238)	22(176) 404(334)	−331(205) 735(209)	*Y*
Cr XXIII $1s^2-1s2p$	2.1821	−153(169) 852(220)	−476(129) 341(353)	−544(158) 732(225)	−343(127) 497(169)	*Y*
Ca XX $1s-3p$	2.5494	−283(146) 364(183)	−357(214) 442(294)	−296(102) 345(160)	−776(145) 544(182)	*Y*
Ca XX $1s-2p$	3.0203	−414(34) 393(48)	−417(37) 422(45)	−494(34) 388(45)	−436(33) 356(49)	*Y*
Ca XIX $1s^2-1s2p$	3.1772	−391(48) 248(77)	−395(50) 248(88)	−547(58) 198(146)	−427(46) 178(110)	*Y*
Ar XVIII $1s-2p$	3.7329	−431(25) 303(34)	−383(32) 476(47)	−442(31) 335(42)	−468(26) 323(35)	*Y*
S XVI $1s-3p$	3.9912	−420(32) 256(50)	−464(39) 242(58)	−507(37) 197(72)	−433(34) 219(59)	*Y*
S XVI $1s-2p$	4.7292	−421(36) 586(49)	−520(35) 504(46)	−533(25) 347(30)	−355(23) 369(29)	*Y*
S XV $1s2-1s2p$	5.0387	−359(32) 85(66)	−348(41) 132(92)	−415(40) 90(69)	−526(96) 309(143)	*Y*
Si XIV $1s-3p$	5.2172	−360(30) 279(41)	−437(31) 229(45)	−545(34) 294(46)	−470(23) 205(36)	*Y*
Si XIV $1s-2p$	6.1822	−446(10) 311(13)	−464(11) 300(14)	−483(11) 370(14)	−453(10) 303(13)	*Y*
Si XIII $1s^2-1s2p$	6.6480	−343(29) 185(46)	−335(32) 233(40)	−375(25) 171(44)	−373(33) 196(41)	*Y*
Mg XII $1s-7p$	6.4486	−408(27) 139(37)	−395(21) 82(63)	−412(34) 187(46)	−411(28) 176(41)	*Y*
Mg XII $1s-5p$	6.5801	−510(17) 164(28)	−502(16) 146(24)	−510(17) 178(24)	−521(20) 191(31)	*Y*
Mg XII $1s-3p$	7.1062	−365(16) 91(31)	−406(17) 114(25)	−398(20) 114(32)	−381(18) 61(49)	*Y*
Mg XII $1s-2p$	8.4210	−410(9) 339(11)	−427(9) 278(10)	−467(9) 259(10)	−471(10) 263(12)	*Y*
Ne X $1s-4p$	9.7082	−359(25) 151(46)	−390(21) 107(39)	−439(19) 95(30)	−399(21) 141(32)	*Y*
Na XI $1s-2p$	10.0250	−346(19) 166(26)	−339(19) 146(25)	−443(22) 151(27)	−441(20) 127(26)	*Y*
Ne X $1s7p$	9.2912	−418(63) 84(93)	−447(52) 93(84)	−380(74) 199(63)	−391(46) 100(80)	*Y*
Ne X $1s-6p$	9.3616	−776(25) 287(31)	−846(25) 291(32)	−837(34) 250(45)	−945(32) 114(47)	*N*
Ne X $1s-5p$	9.4807	−365(28) 247(32)	−322(28) 194(34)	−370(27) 222(34)	−391(26) 201(33)	*Y*
Ne X $1s-3p$	10.2389	−363(18) 222(25)	−439(20) 229(22)	−407(15) 143(21)	−449(16) 207(20)	*Y*
Ne X $1s-2p$	12.1330	−441(21) 281(25)	−420(21) 225(25)	−452(20) 236(26)	−482(17) 213(27)	*Y*
Ne II	14.6310	−389(34) 182(42)	−393(33) 132(46)	−410(30) 82(73)	−457(46) 223(49)	*Y*
O VIII $1s-4p$	15.1762	−296(90) 361(113)	−329(81) 314(133)	−471(68) 186(101)	−374(42) 41(73)	*Y*
O VIII $1s-3p$	15.9870	−23(63) 151(90)	−9(77) 234(79)	−110(74) 182(111)	−2(80) 200(94)	*N*

Mon. Not. R. Astron. Soc. **000**, 1–?? (2011) Printed 18 January 2012 (MN LATEX style file v2.2)

Measuring the black hole masses in accreting X-ray binaries by detecting the Doppler orbital motion of their accretion disk wind absorption lines

Shuang-Nan Zhang [1, 2], Jinyuan Liao [1], Yangsen Yao [3⋆]
[1] *Key Laboratory of Particle Astrophysics, Institute of High Energy Physics, Chinese Academy of Sciences, Beijing 100049, China*
[2] *Space Science Division, National Astronomical Observatories of China, Chinese Academy of Sciences, Beijing 100012, China*
[3] *Center for Astrophysics and Space Astronomy, University of Colorado, Boulder, CO 80309, USA*

arXiv:1201.3451v1 [astro-ph.HE] 17 Jan 2012

Accepted date. Received date

ABSTRACT

So far essentially all black hole masses in X-ray binaries have been obtained by observing the companion star's velocity and light curves as functions of the orbital phase. However a major uncertainty is the estimate of the orbital inclination angle of an X-ray binary. Here we suggest to measure the black hole mass in an X-ray binary by measuring directly the black hole's orbital motion, thus obtaining the companion to black hole mass ratio. In this method we assume that accretion disk wind moves with the black hole and thus the black hole's orbital motion can be obtained from the Doppler velocity of the absorption lines produced in the accretion disk wind. We validate this method by analyzing the Chandra/HETG observations of GRO J1655–40, in which the black hole orbital motion ($K_{\rm BH} = 90.8 \pm 11.3$ km s^{-1}) inferred from the Doppler velocity of disk-wind absorption lines is consistent with the prediction from its previously measured system parameters. We thus estimate its black hole mass ($M_{\rm BH} = 5.41^{+0.98}_{-0.57}\ M_\odot$) and then its system inclination ($i = 72.0^{+7.8}_{-7.5}\ ^\circ$), where $M_{\rm BH}$ does not depend on i. Additional observations of this source covering more orbital phases can improve estimates on its system parameters substantially. We then apply the method to the black hole X-ray binary LMC X–3 observed with HST/COS near orbital phase 0.75. We find that the disk-wind absorption lines of C IV doublet were shifted to $\sim$ 50 km s^{-1}, which yields a companion-to-black-hole mass ratio of 0.6 for an assumed disk wind velocity of -400 km s^{-1}. Additional observations covering other orbital phases (0.25 in particular) are crucial to ease this assumption and then to directly constrain the mass ratio. This method in principle can also be applied to any accreting compact objects with detectable accretion disk wind absorption line features.

1 INTRODUCTION

Black holes (BHs) are believed to exist in many X-ray binaries (XRBs) and active galactic nuclei (AGN). Measurement of the motion of a BH with respect to its surrounding in such a system can in principle set strong constraints on the mass of the BH. However in an AGN this is normally not possible because the time scale of BH's significant motion is too long and/or the BH is barely moving at all. In an XRB, the BH should move with respect to the system's center of mass (CM), making it possible to detect directly the BH's motion with respect to the CM. However in a low-mass XRB (LMXB) the companion is normally much less massive than the BH, so that the BH barely moves or moves very slowly with respect to the CM. In some LMXBs, the companion's mass is comparable or only several times less massive than the BH, e.g., in GRO J1655–40 (Zhang et al. 1994; Orosz & Bailyn 1997), the BHs' motion may be significant enough for direct detection. The most favorable systems for detecting BH's motion should be high-mass XRBs (HMXBs), in which the BHs move rapidly with respect to their CMs.

Orbital motion of double-peaked disk emission lines were observed for neutron star XRB Sco X–1 (Steeghs & Casares 2002), the BH XRB A0620–00 (Haswell & Shafter 1990; Orosz et al. 1994), and the BH GRS 1124–68 (Orosz et al. 1994). Unfortunately a significant phase offset of velocity modulation was found from that expected based on the observed orbital motion of the companion, though the velocity semi-amplitude is consistent with the expected mass ratio (Orosz et al. 1994). Soria et al. (1998) observed the orbital motion of the double-peaked disk emission line He II λ4686 from GRO J1655–40, and found its velocity modulation phase and semi-amplitude in agreement with the kinematic and dynamical parameters of the system. Therefore a more robust mass lower limit is placed

based on the observed motion of the primary and thus ruling out any possibility for a neutron star as the primary in the system (Soria et al. 1998). However one major problem in accurately measuring the orbital motion of the primary from the observed double-peaked emission lines is how to determine reliably the line center, because the lines are typically asymmetric and also variable.

In an XRB, both the accretion disk and its wind move with the BH, and thus provides us with another opportunity to measure the BH's motion via Doppler shift of absorption features of the accretion disk wind. Accretion disk winds are ubiquitous in XRBs and normally detected through ionized absorption lines, typically with around $\sim 10^3$km s^{-1} or less (e.g., Ueda et al. 2004; Miller et al. 2004, 2006, 2008), but can reach to about $\sim 10^4$km s^{-1} in some extreme cases, e.g. in the newly discovered BH transient IGR J17091–3624 (King et al. 2011). In particular the high quality Chandra/HETG observations of the BHXB GRO J1655–40 have found many highly ionized narrow absorption lines, which are interpreted as evidence of magnetic field-driven accretion disk wind (Miller et al. 2006; Kallman et al. 2009; Luketic et al. 2010); although the absorption lines are also interpreted as from the absorption by X-ray heated thermal wind (Netzer 2006). Regardless the origin of the accretion disk wind, the orbital motion of its many absorption lines may be measured reliably, because typically many narrow absorption lines are present with high signal to noise ratios and appear to be rather stable when observed.

In this work, we model the Doppler motion of wind absorption lines from the LMXB GRO J1655–40 and HMXB LMC X–3 to constrain directly the companion to primary mass ratio, in order to measure their BH masses and orbital inclination angles. We first describe the methodology and test its feasibility by applying it to Chandra/HETG observations of GRO J1655–40, revealing for the first time the velocity modulation of wind absorption lines in an XRB and thus providing a new measurement of its BH motion and orbital inclination angle. We then apply this method to the HST/COS observations of LMC X–3 attempting to constrain the companion to primary mass ratio. Finally we discuss further observations needed to achieve the required accuracy of BH mass estimate for LMC X–3, as well as potential problems and uncertainties of applying this method.

2 METHODOLOGY

So far, all BH masses in XRBs have been estimated using the Kepler's 3rd law of stellar motion, expressed in the so called the mass function,

$$f(M) \equiv P_{\rm orb}K_{\rm C}^3/2\pi G = M_{\rm BH}\sin^3 i/(1+q)^2, \qquad (1)$$

where $P_{\rm orb}$ is the orbital period, $K_{\rm C}$ is the semi–amplitude of the velocity curve of the companion star, $M_{\rm BH}$ is BH mass, i is the the orbital inclination angle, and $q \equiv M_{\rm C}/M_{\rm BH}$ is the mass ratio. Since the only direct observables are $P_{\rm orb}$ and $K_{\rm C}$, both $M_{\rm C}$ and i have to be determined indirectly in order to obtain the BH mass estimate reliably. The companion's mass $M_{\rm C}$ can be determined relatively reliably by the observed spectral type of the companion star. For LMXBs, i can be estimated by modeling the optical or infrared light curve modulation, though model dependence and other uncertainties (such as accretion disk contamination) cannot be circumvented completely. For HXMBs, i is normally not determined very well; in many cases observations or lack of eclipse of the accretion disk emission by the companion is used to put some constraints on the possible ranges of i. For details of BH mass estimates using this method, please refer to Remillard & McClintock (2006).

On the other hand, the mass ratio q can be determined directly according to the law of momentum conservation, i.e.,

$$M_{\rm C}/M_{\rm BH} = K_{\rm BH}/K_{\rm C}, \qquad (2)$$

if the semi–amplitude of the velocity curve of the BH $K_{\rm BH}$ can be observed directly. Since a BH is not directly observable, we can only hope to observe any emission or absorption line feature co-moving with it. The accretion disk certainly moves with the accreting BH. However any line feature of the inner accretion disk suffers from the broadening of disk's orbital motion and distortions by relativistic effects around the BH, thus making it practically impossible, or difficult to the least, for detecting the binary orbital motion of the BH. Emission line features from the outer disk region are normally detected with double-peaks, which can be modeled to obtain the semi–amplitude of the velocity of the compact object, as discussed above. However a major uncertainty is to determine the mean separation between the emission regions of the blue-shifted and red-shifted components.

Fortunately, as we have discussed above, absorption line features of accretion disk winds in BHXBs have been routinely detected with high significance. This suggests that the accretion disk wind in an XRB moves with the disk that produces the wind, since otherwise the wind from the disk would not intercept the continuum emissions produced from the same disk. In this case, the Doppler motion of wind absorption line features can be considered as that of the BH, unless the wind interacts strongly with the surrounding interstellar medium or the wind intrinsic velocity has systematic orbital dependence. It has been found recently that large scale (pc) cavities exist around microquasars (XRBs producing relativistic jets), and perhaps are ubiquitous in all BHXBs producing strong winds (Hao & Zhang 2009). This suggests that at least in the vicinity of the BH the wind cannot interact directly with interstellar medium. The interactions of disk winds with interstellar medium at pc scale would not complicate the observations, because it takes much longer than an orbital period before the winds could arrive at the boundaries of these cavities, and thus the wind should have lost any possible memories of the orbital motion of the compact object. For disk-fed accretion, the wind velocity is not expected to have any orbital phase modulation; for stellar-wind accretion the focused wind may complicate the situation considerably though. We therefore suggest to apply this method to only those systems in which the accretion is disk-fed, i.e., no significant wind interaction happens between the stellar and accretion disk winds. Nevertheless only observations can tell us in which kinds of systems this method can be used reliably.

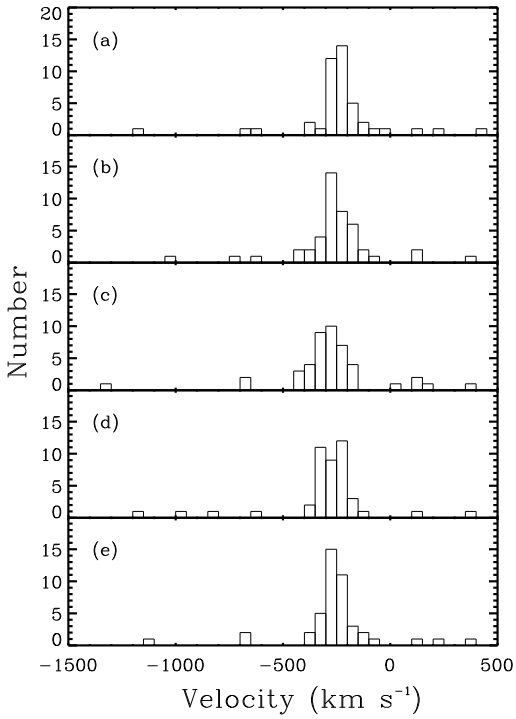


Figure 1. Distributions of the line velocities in four equally spaced intervals and their average values, during the Chandra/HETG observations lasting for more than 60 ksec; note that here the system velocity of the BH XRB has already been subtracted. Panels from (a) to (d) corresponding to the phases shown in Fig. 2 from left to right.

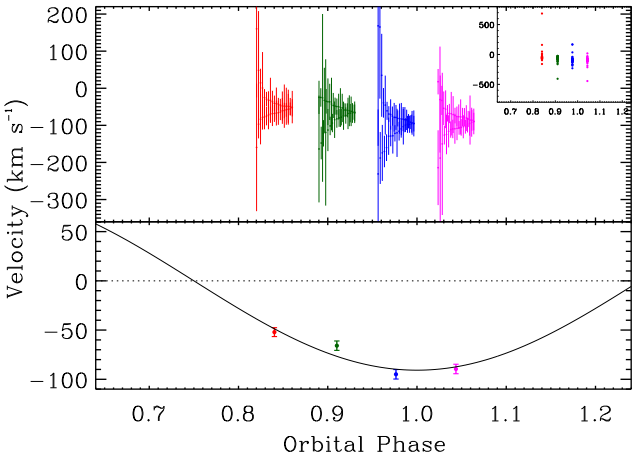


Figure 2. Velocity curve of the 39 observed absorption lines, after rejecting six lines as suspected outliers and subtracting the line of sight intrinsic velocity of each line at each orbital phase. The upper panel marks the velocity of each line with its 1-σ error bar slightly shifted horizontally for visual clarity; the inset shows all velocities, including the three data points out of the range in the main panel. The bottom panel shows the weighted average velocity of all lines in the upper panel at each phase; the solid curve is the fitted velocity curve with its orbital period and phase fixed at the values observed previously.

3 APPLICATION TO THE LMXB GRO J1655–40: A TEST STUDY

GRO J1655–40, discovered as an X-ray transient by Zhang et al. (1994), is a well-known and best studied BHXB and the second source with superluminal relativistic jets detected (Tingay et al. 1995; Harmon et al. 1995; Hjellming & Rupen 1995). Its system parameters remain so far the best measured among all known BHXBs, with $P_{\rm orb} = 2.62191 \pm 0.00020$ d, $1/q \equiv M_{\rm BH}/M_{\rm C} = 2.6 \pm 0.3$, $i = 70.2 \pm 1.9^\circ$, and $M_{\rm BH} = 6.3 \pm 0.5\ M_\odot$ (all 95% confidence) (Orosz & Bailyn 1997; Greene et al. 2001). Its precise BH mass and inclination measurements allow its BH spin parameter determined from its X-ray continuum fitting, first proposed by Zhang et al. (1997) and then refined by incorporating detailed modeling of various effects (e.g., Yao et al. 2005; Li et al. 2005; Davis et al. 2005; Shafee et al. 2006; Steiner et al. 2009; McClintock et al. 2011). However possible sources of systematic errors are in the modeling of the ellipsoidal light modulation of the companion star and contamination of the disk's continuum emission in the optical to infrared bands. Soria et al. (1998) observed the velocity curve of the double-peaked disk emission line He II λ4686 from GRO J1655–40, and derived its projected radial velocity semi-amplitude determined for the primary as $K_{\rm BH} = 76.2 \pm 7.5$ km s^{-1}, yielding $M_{\rm BH} = 6.62 \pm 0.74\ M_\odot$ and $i = 66.6 \pm 7.7^\circ$ (all 68.3% confidence), fully consistent with that determined from the companion's velocity curve and ellipsoidal light variation.

Miller et al. (2006) detected many narrow and ionized absorption lines with High Energy Transmission Grating (HETG) Chandra observations of GRO J1655–40. The exact position of the point source cannot be determined accurately in the zeroth order image, which is severely piled-up due to its high flux. An offset in the source position will cause a systematic shift of all lines in the wavelength space. However, this shift is mostly canceled out in the combined total spectrum if each line is detected in the spectra of both the $+1$ and -1 orders with similar count spectra. However the combined lines will be broadened by the unknown systematic offset, which in turn will cause larger uncertainties in determining the center of each line. There may also exist other sources of systematic errors which can cause offset between the centers of the same line in the spectra of the $+1$ and -1 orders.

Here we determine the position of the zeroth order image by minimizing the relative offsets between the absorption lines in the $+1$ and -1 orders, and estimate the systematic error in determining the center wavelength of each absorption line. We first fit each absorption line feature with a Gaussian profile in the $+1$ and -1 orders of the High Energy Grating (HEG) and Medium Energy Grating (MEG) separately, i.e., we get a pair of profiles for each absorption line, integrated over the whole observation in order to get the highest signal to noise ratio. The local continuum around each line is assumed to have a power-law shape, but our results are insensitive to the continuum shape. For HEG and MEG we obtain 43 and 9 pairs of absorption lines with at least 3-σ detection, resulting in 43 and 9 differences of the central wavelengths of these pairs, respectively. We then use the Bayesian method to find the offset d and its systematic

error $\sigma_{\rm s}$ by maximizing the following function,

$$p(d,\sigma_{\rm s}) = \frac{1}{\sqrt{(2\pi)^n}} \prod \frac{1}{\sqrt{{\sigma_{x_k}}^2+\sigma_{\rm s}^2}} e^{-\frac{(d-x_k)^2}{2({\sigma_{x_k}}^2+\sigma_{\rm s}^2)}}, \quad (3)$$

where x_k and σ_{x_k} are the wavelength difference and its statistical error of the k-th pair ($k = 1$ to n, and $n = 43$ for HEG or 9 for MEG), respectively. Finally for HEG we get $d = (4.8 \pm 0.1) \times 10^{-3}$ Å and $\sigma_{\rm s} = (3.2 \pm 1.3) \times 10^{-4}$ Å.

We thus take the error for d as $\sigma_d = \sigma_{\rm s} = 3.2 \times 10^{-4}$ Å for HEG. Similarly for MEG we get $d = (9.7 \pm 0.8) \times 10^{-3}$ Å for MEG, where $\sigma_d = 9 \times 10^{-4}$ Å is dominated by the systematic error. Taking these additional errors for MEG and HEG line wavelengths and requiring all pairs in HEG with $d = 4.8 \times 10^{-3}$ Å and in MEG $d = 9.7 \times 10^{-3}$ Å, we have a total $\chi^2 = 55$ for 50 degrees of freedom, thus validating our method of determining the systematic errors. Since the wavelength bin (an image pixel) is 2.5×10^{-3} Å or 5.0×10^{-3} Å for HEG or MEG, we thus shift the spectra of the -1 and the $+1$ orders by one bin, towards the decreasing (-1 order) and increasing ($+1$ order) wavelength directions, respectively. This is identical to shifting the location of the point source by one pixel in the zeroth order image. Finally we combine the two shifted spectra as one single spectrum.

Because the observations lasted for about a quarter of the orbital phase of GRO J1655–40 and many absorption lines have high signal to noise ratios, here we divide the observations into four equal orbital internals in order to detect the orbital motion of the absorption lines. For each combined spectrum we again fit each absorption feature with a Gaussian profile to determine its central wavelength, line width and intensity. Table 1 lists the 45 lines in all four intervals with at least 3-σ detection that are included for further analysis; here only statistical errors are shown.

Fig. 1 shows the velocity distributions of the four groups of 45 lines and their average velocities; note that here the system velocity of the BH XRB has already been subtracted. Adopting the orbital period and phase ephemeras from Greene et al. (2001) and assuming that the BH's motion is exactly anti-phased with the companion's motion (Soria et al. 1998), we fit velocities of these lines simultaneously to a sinusoidal function. In the fit, the intrinsic velocity of each line is a free parameter, but all lines in the same orbital phase follow the same orbital modulation. This way we have 46 free parameters (45 intrinsic velocities for all these lines plus the line of sight velocity amplitude of the black hole) with 180 data points. The fit results in $K_{\rm BH} = 93.8 \pm 11.1$ km s^{-1} with $\chi^2 = 179$ for 134 degrees of freedom; the systematic errors determined above are included for all lines.

Considering that some lines may be outliers, we reject the four groups of six lines with central velocities more than 300 km s^{-1} from the median values of each distribution, as listed in Table 1. The remaining four groups of 39 lines have velocity dispersion (1-σ) of about 60 km s^{-1}, i.e., the rejected lines are more than 5-σ away from the median values. The fit to the remaining four groups of 39 lines yields $K_{\rm BH} = 90.8 \pm 11.3$ km s^{-1} with $\chi^2 = 131$ for 116 degrees of freedom, a marginal improvement over the full dataset fit. This means that the deviations of these possible outliers are not significant statistically and thus do not deserve further studies at this stage. Fig. 2 shows the fitting results; please note that the velocities are obtained by subtracting the fitted line of sight intrinsic velocity of each line from the obtained central velocity of each line at this orbital phase. It is worth noting that the phase zero in this system was defined as that when the companion is receding from the observer at the maximum velocity (Orosz & Bailyn 1997). Nevertheless both results are statistically consistent with $K_{\rm BH} = 76.2 \pm 7.5$ km s^{-1} obtained by Soria et al. (1998). If we fit the four groups of 39 lines to a straight line, we get $\chi^2 = 813$ for 154 degrees of freedom. The linear model is thus rejected with high significance, compared to the sinusoidal model.

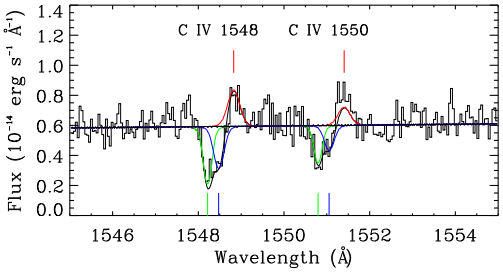


Figure 3. Spectrum of the available HST/COS observations around C IV doublet. Red curves indicate the fit to the emission from the heated surface of the companion star, green curves are the fit to the Galactic ISM absorptions at 0 km s^{-1} , and blue curves indicate the fit to the accretion disk wind absorptions at $\approx$ 50 km s^{-1} (local velocity ≈ -400 km s^{-1}). The vertical bars mark the central positions of these components.

With the fitted $K_{\rm BH} = 90.8 \pm 11.3$ km s^{-1} and taking the other system parameters (except the inclination) of GRO J1655–40 from Greene et al. (2001), we first obtain its BH mass $M_{\rm BH} = 5.41^{+0.98}_{-0.57}$ $M_\odot$ from Eq. 2 and then its system inclination $i = 72.0^{+7.8}_{-7.5}$ ° from Eq. 1, respectively. All these (1-σ) errors are obtained by Monte-Carlo samplings, because of the asymmetry and coupling of some errors. These parameters, albeit with large uncertainties due to the very incomplete orbital coverage of observations, are consistent with all previous measurements. Therefore the existing data of GRO J1655–40 validate our proposal that absorption lines produced in the accretion disk wind can be used to measure directly the orbital motion of the BHs in BHXBs.

4 APPLICATION TO THE HMXB LMC X–3

LMC X–3 is another excellent object for applying this method. It is a bright XRB system in the Large Magellanic Cloud composed of a B3 V star and a central BH, and receding away from us at a systemic velocity $V_{\rm S} = +310$ km s^{-1} (Cowley et al. 1983; hereafter C83). It is one of the few BH systems that are persistently luminous in both X-ray and far-ultraviolet (FUV) wavelength bands. The BH is believed to be undergoing accretion from its B-star companion via Roche lobe overflow with an orbital period of 1.7 days (C83); we therefore do not expect any significant contamination of the stellar wind to any absorption features of its accretion disk wind. Spectroscopic observations of

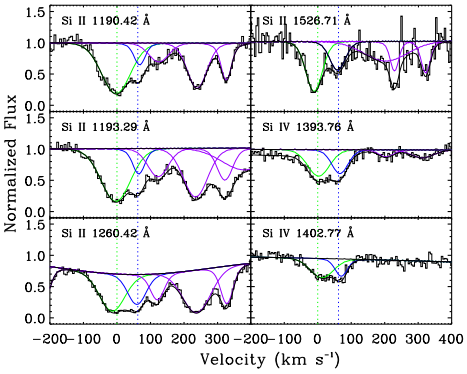


Figure 4. Si II and Si IV absorption features in the spectrum of the previous HST/COS G130M observations, normalized to the continuum flux. The apparent higher velocity components (marked with pink curves) may be produced in the outer part of the disk wind at lower local velocities.

the B star indicate a large radial velocity semi-amplitude, $K_{\rm C} = 235 \pm 11$ km s^{-1} (C83). Taken the mass of the B3 V star as about 6 $M_{\odot}$, the BH mass in LMC X–3 is thus estimated to be $5 - 10$ $M_{\odot}$, assuming an inclination angle of $50^{\circ} - 70^{\circ}$ (C83; Kuiper et al. 1988; Soria et al. 2001). Because of the considerable uncertainty in its inclination (and thus BH mass), its BH spin has not been reliably determined yet with the X-ray continuum modeling method (e.g., Zhang et al. 1997; Steiner et al. 2010). Since the BH should be moving at a comparable velocity to its companion, it is possible to directly measure its orbital motion if the absorption lines produced in its accretion disk wind are detected.

Although LMC X–3 has been intensively studied in the X-ray band, the previously operated and currently operating X-ray spectroscopic instruments lack the combination of the required sensitivity and resolution to measure the expected Doppler motion of any accretion wind absorption features. High resolution UV spectroscopic observations of this source are rather sparse; so far only two *FUSE* observations and four observations with the Cosmic Origins Spectrograph (COS) onboard the *Hubble Space Telescope* (HST) (HST/COS hereafter) to LMC X–3 have been made (Hutchings et al. 2003; Wang et al. 2005; Song et al. 2010, here after S10). Again *FUSE* does not have the combination of the required sensitivity and the observations did not produce spectra with high enough signal to noise ratio for the purpose of this investigation. The HST/COS does have the required performance to do so, although the available observations only covered a small portion of the orbital period of LMC X–3. In this work, we analyze the available HST/COS UV spectroscopic observations of LMC X–3, aiming at constraining the systemic parameters and further demonstrating the feasibility of our proposed new method of measuring the BH's mass in an XRB.

From the *FUSE* and HST/COS observations, S10 detected variable O VI and N V emission lines and found that variability of their intensities are inconsistent with expectation of a stellar wind origin. So they attributed them to the heated stellar surface of the companion star. In fact both absorption and emission features are detected in N V (with G130M) and C IV (with G160M) doublets (Fig. 2 in S10) in the HST/COS observations (Program 11642; please refer to S10 for detailed description of the HST/COS observations and data analysis). However, since S10 focused on the origin of the emission variability and the connection between the emission features and the systemic parameters, these absorption features have not been explored in detail.

Here we analyze the C IV doublet complexes (we do not conduct the same analysis to the N V features because the absorptions are much less significant than those of C IV). In Fig. 3, we decompose the observed C IV doublet into three components for each line: one emission component and two absorption components. The emission component is assumed to come from the heated surface of the companion, the same as the O VI and N V emission lines (S10); its width and Doppler shift are fixed to those inferred from the O VI and N V emission lines in the decomposition. One absorption component (at zero velocity) is assumed to come from the Galactic ISM absorption. The other significant absorption component has a redshift of about 50 km s^{-1}, and may have two possible origins. One is the absorption produced in the stellar wind of the B3 V companion star. However, the orbital phase of the binary system was about 0.75 during the HST/COS observations, i.e., the straight line connecting the companion star and the BH is perpendicular to our LOS (please be noted that, in contrast to GRO J1655–40, the orbital phase zero in LMC X–3 was defined as that when the BH is at its superior conjunction, i.e., the companion is just between the observer and the BH; Cowley 1983; S10). In order for any stellar wind to intercept significantly the emission from the inner disk region, a significant amount of stellar wind has to stream to the inner disk region, i.e., the system must be wind-fed, against the common believe that LMC X–3 is actually disk-fed. We thus rule out this possibility. The other and the only viable scenario is the absorption by the accretion disk wind, making it possible to directly measure the orbital motion of the BH. It is worth noting that the measured C IV column density in the ISM [$\log N_{\rm ISM}({\rm cm}^{-2}) = 13.7 \pm 0.1$] agrees remarkably well with predicted value [$\log N_{\rm CIV}({\rm cm}^{-2}) = 13.8$] in a joint analysis of the X-ray and FUV spectroscopic observations of LMC X–3 (Yao et al. 2009), indirectly validating such a component decomposition.

With the measured velocity $V_{0.75} = 51.3 \pm 4.1$ km s^{-1} of C IV absorption lines tracing the BH motion and considering the systemic velocity ($V_{\rm S} = +310$ km s^{-1}) of LMC X–3 and velocity semi-amplitude of the companion star $K_{\rm C} = 235$ km s^{-1}, we can constrain the companion to black hole mass ratio. At phase 0.75, the BH is receding from us at the maximum speed, and thus the relation of $V_{0.75}$ and $K_{\rm BH}$ can be expressed as

$$V_{0.75} = V_{\rm wind} + V_{\rm S} + K_{\rm BH}, \qquad (4)$$

where $V_{\rm wind}$ is the intrisinc velocity of the accretion disk wind in our LOS. Assuming $V_{\rm wind} = -400$ km s^{-1}, a similar wind velocity found in GRO J1655–40 (Miller et al. 2006), from Eq. 4 we obtain $K_{\rm BH} \sim 140$ km s^{-1}. Plugging these numbers in Eq. 2, we further obtain $q = M_C/M_{\rm BH} \sim 0.6$, which is consistent with the ratio usually adopted for the LMC X–3 system (e.g., C83). We therefore suggest that the observed C IV absorption feature is consistent to our model that the accretion disk wind moves with the BH and the observed Doppler shift is a combination of the wind velocity and the BH's orbital velocity in our LOS.

In the above exercise, we assumed a $V_{\rm wind}$ in order to obtain $K_{\rm BH}$, since there is a degeneracy of $V_{\rm wind}$ and $K_{\rm BH}$ in Eq. 4. Unfortunately, the HST/COS G160M observation analyzed above only lasted for one HST orbit, and thus cannot break the degeneracy, i.e., we cannot put an independent measure of the BH's velocity, without observing the orbital modulation of the Doppler motion of the wind. The HST/COS G130M observations in a shorter wavelength band covered a much larger part of the orbital period. As shown in Fig. 4, the combined spectrum revealed several complicated absorption features. Nevertheless, Si II and Si IV absorption lines at $V_{0.75} \approx 50$ km s^{-1} are also detected; the apparent higher velocity components may arise from the outer part of the accretion disk with lower local velocities, mimicking the different velocities and ionization zones of AGN warm-absorbers/outflows (e.g., Arav et al. 2005). However, the combination of the complexity of the observed absorption features and the rather incomplete orbital phase coverage of these previous HST/COS observations does not warrant further more quantitative analysis for breaking the above mentioned degeneracy and probing the nature of those higher velocity components.

Clearly, observations covering more orbital phases are badly needed to break the degeneracy. Observations around phase 0.25 are the most favorable ones for this purpose. In contrast to the existing observations taken around 0.75 in which the BH is receding at the maximum velocity from us, at phase 0.25, the BH is expected to be moving toward us at the maximum velocity, so is the disk wind. Therefore, the relation between $V_{0.25}$ and $K_{\rm BH}$ can be expressed as

$$V_{0.25} = V_{\rm wind} + V_{\rm S} - K_{\rm BH}. \quad (5)$$

If $V_{\rm S} = -400$ km s^{-1} as assumed, the $V_{0.25}$ is expected to be at -230 km s^{-1}. The real measurement of $V_{0.25}$ from the future observations, together with $V_{0.75}$ measured from the existing observations, would allow us to solve $V_{\rm wind}$ and $K_{\rm BH}$ from Eqs. 4 and 5 and then to reliably constrain $M_C/M_{\rm BH}$ and system inclination angle i (Eqs. 2 and 1).

5 SUMMARY AND DISCUSSION

As shown in Eq. 2, $M_{\rm BH}$ can be directly obtained if $K_{\rm BH}$ can be measured, in addition to $M_{\rm C}$ and $K_{\rm C}$ measured by observing the companion star. In this work we suggest to measure $K_{\rm BH}$ by detecting the Doppler orbital motion of the accretion disk wind absorption lines, assuming that the accretion disk wind moves with the BH and does not have systematic orbital phase dependence. This method has the potential of circumventing the model dependence and other uncertainties in estimating the orbital inclination angle, that is required in the method commonly used to measure the BH masses in XRBs by detecting the companion star's velocity and light curves, as shown in Eq. 1. Actually knowing the mass ratio with Eq. 2, one can in turn use Eq. 1 to derive the inclination angle, which can be used to calibrate the light curve model used previously to derive the inclination angle.

Our analysis of the previous Chandra/HETG observations of GRO J1655–40 have revealed wind velocity modulation consistent with the orbital motion of the BH predicted from its previously measured system parameters. An independent projected radial velocity semi-amplitude measured here allows its inclination angle determined without using the modeling of its ellipsoidal light modulation of its companion. We find its BH radial velocity semi-amplitude $K_{\rm BH} = 90.8 \pm 11.3$ km s^{-1}, BH mass $M_{\rm BH} = 5.41^{+0.98}_{-0.57}\ M_\odot$ and system inclination $i = 72.0^{+7.8}_{-7.5}\ ^\circ$, where $M_{\rm BH}$ does not depend on i at all. However the very limited orbital coverage of the observations does not allow more accurate system parameter measurements of this binary system. Nevertheless with the velocity component of its orbital motion removed, we can obtain more accurate measurements of the intrinsic velocities of each line along our line of sight, and thus may be able to constrain further the physical properties of the wind, by combining with the velocity broadenings of these lines; this is the subject our future work.

Our analysis of the previous HST/COS observations of the HMXB LMC X–3 has found absorption line features consistent with that predicted by assuming the previously measured dynamical parameters of LMC X–3 and the wind properties in LMC X–3 being similar to that observed in another BHXB GRO J1655–40. Given the limitations of the previous HST/COS observations of LMC X–3 that do not allow to break the degeneracy of the wind velocity and the BH orbital velocity, new HST/COS observations are required to cover significantly different orbital phases.

As mentioned in S10, the C IV features shown in Fig. 3 might be P-cygni profiles. However, the emission features agree well with all other emission lines detected, which are attributed to the heated stellar surface. Therefore it is more reasonable to attribute the emission features in Fig. 3 to the heated stellar surface (as done in S10), thus invalidating the P-cygni profile interpretation. UV emission lines produced from the heated stellar surface are not unique in the system of LMC X–3, but rather a common feature observed in XRBs (e.g., Vrtilek et al. 2003). Of course new observations suggested above would definitely reveal the nature of the the C IV features shown in Fig. 3.

In this work, we have also assumed that the accretion disk wind velocity is constant, at least during one full orbital phase, in order to apply this method reliably. In reality, the intrinsic wind velocity may have random fluctuations, though the fluctuations do not seem to be significant in GRO J1655–40 (Miller et al. 2006). However, it has been known that wind absorption features are not always detected and it is also not fully understood when and why wind absorptions are present or absent. Future high signal to noise observations covering more orbital phases may shed some lights on this problem and test ultimately if our suggested method can be applied reliably and produce accurate BH mass measurements in BHXBs. The joint JAXA/NASA *ASTRO-H* mission is particularly suitable for making such observations, with its high-throughput spectroscopy provided by the micro-calorimeter with high spectral resolution of $\Delta E \sim 7$ eV (Takahashi et al. 2010). Finally we should point out that this method in principle can also be applied to other accreting compact objects, such accreting neutron star and white dwarf binaries, with detectable accretion disk wind absorption line features.

ACKNOWLEDGMENTS

S.N.Z. thanks the hospitality of CASA, University of Colorado at Boulder, during his visit in December 2010 when the initial idea of this work emerged as results of some interesting discussions with local scientists there. The anonymous referee is thanked for making several useful comments and suggestions. We appreciate comments and suggestions made by Drs. Zhongxiang Wang and Hua Feng. Daniel Dewey is thanked for his information and suggestion on evaluating the systematic errors. S.N.Z. also acknowledges partial funding support by the National Natural Science Foundation of China under grant nos. 11133002, 10821061, 10725313, and by 973 Program of China under grant 2009CB824800. Y.Y. appreciates financial support by NASA through grant HST-GO-11642.01-A.

REFERENCES

Arav, N., et al. 2005, ApJ, 620, 665
Boyd, P. T., et al. 2001, 555, 822
Begelman, M. C., et al. 1983, ApJ, 271, 70
Cowley, A. P., et al. 1983, ApJ, 272, 118 (C83)
Cowley, A. P., et al. 1994, ApJ, 429, 826
Davis, S. W., Blaes, O. M., Hubeny, I., & Turner, N. J. 2005, ApJ, 621, 372
Greene, J., Bailyn, C. D., & Orosz, J. A. 2001, ApJ, 554, 1290
Hao, J. F., & Zhang, S. N. 2009, ApJ, 702, 1648
Harmon, B. A., Wilson, C. A., Zhang, S. N., et al. 1995, Nature, 374, 703
Haswell, C. A., & Shafter, A. W. 1990, ApJ, 359, L47
Hjellming, R. M., & Rupen, M. P. 1995, Nature, 375, 464
Hutchings, J. B., et al. 2003, AJ, 126, 2368
Kallman T. R., Bautista M. A., Goriely S., Mendoza C., Miller J. M., Palmeri P., Quinet P., Raymond J., 2009, ApJ, 701, 865
King A. L., et al., 2012, ApJL, in press, arXiv:1112.3648
Kuiper, L., et al. 1988, A&A, 203, 79
Li, L.-X., Zimmerman, E. R., Narayan, R., & McClintock, J. E. 2005, ApJS, 157, 335
Luketic, S., et al. 2010, ApJ, 719, 515
McClintock, J. E., Narayan, R., Davis, S. W., et al. 2011, Classical and Quantum Gravity, 28, 114009
Miller, J. M., et al. 2004, ApJ, 601, 450
Miller, J. M., et al. 2006, Nature, 441, 953
Miller, J. M., et al. 2008, ApJ, 680, 1359
Netzer, H. 2006, ApJ, 652, L117
Orosz, J. A., Bailyn, C. D., Remillard, R. A., McClintock, J. E., & Foltz, C. B. 1994, ApJ, 436, 848
Orosz, J. A., & Bailyn, C. D. 1997, ApJ, 477, 876
Remillard, R. A., & McClintock, J. E. 2006, ARA&A, 44, 49
Shafee, R., McClintock, J. E., Narayan, R., et al. 2006, ApJ, 636, L113
Song, L., et al. 2010, AJ, 140, 794
Soria, R., Wickramasinghe, D. T., Hunstead, R. W., & Wu, K. 1998, ApJ, 495, L95
Soria R., et al. 2001, A&A, 365, L273
Steeghs, D., & Casares, J. 2002 ApJ, 1, 273
Steiner, J. F., McClintock, J. E., Remillard, R. A., Narayan, R., & Gou, L. 2009, ApJ, 701, L83
Steiner, J. F., et al. 2010, ApJ, 718, L117
Takahashi, T., Mitsuda, K., Kelley, R., et al. 2010, SPIE, 7732, 77320Z
Tingay, S. J., Jauncey, D. L., Preston, R. A., et al. 1995, Nature, 374, 141
Ueda, Y., et al. 2004, ApJ, 609, 325
Vrtilek, S. D., et al. 2003, PASP, 115, 1124
Wang, Q. D., et al. 2005, ApJ, 635, 386
Yao, Y., Zhang, S. N., Zhang, X., Feng, Y., & Robinson, C. R. 2005, ApJ, 619, 446
Yao, Y., et al. 2009, ApJ, 690, 143
Zhang, S. N., Harmon, B. A., Paciesas, W. S., Wilson, C. A., & Fishman, G. J. 1994, IAUC, 6106, 1
Zhang, S. N., et al. 1997, ApJ, 482, L155

Table 1. Velocity and width of each absorption line at each orbital phase, detected with more than 3-σ significance. For each orbital phase, the numbers in the left and right are the velocity shift and width (broadening) of the absorption line; the $1-\sigma$ errors are included in the parenthesis. The last column indicates if the line is within 300 km s^{-1} to the median velocity at each phase.

Ion and transition	Wavelength (Å)	Phase 1 (km s^{-1})	Phase 2 (km s^{-1})	Phase 3 (km s^{-1})	Phase 4 (km s^{-1})	Within 300 (km s^{-1})
Ni XXVI $1s^22s-1s^25p$	6.1200	−802(48) 102(88)	−756(50) 115(106)	−821(61) 152(90)	−1338(94) 648(86)	*N*
Ni XXVI $1s^22s-1s^24p$	6.8163	−535(33) 380(39)	−560(29) 329(33)	−478(34) 355(42)	−471(33) 355(38)	*Y*
Ni XXVI $1s^22s-1s^23p$	9.0610	−416(12) 212(15)	−431(15) 241(20)	−453(14) 215(18)	−431(14) 220(18)	*Y*
Ni XXVI $1s^22s-1s^23p$	9.1050	−432(16) 168(21)	−432(13) 134(22)	−465(16) 182(23)	−445(18) 179(26)	*Y*
Fe XXVI $1s-2p$	1.7798	−1339(196) 861(239)	−1187(246) 773(261)	−1473(185) 962(207)	−1107(141) 825(154)	*N*
Fe XXV $1s^2-1s2p$	1.8504	74(142) 1408(157)	−38(117) 1167(131)	−11(120) 2070(135)	368(155) 1436(173)	*N*
Fe XXIV $1s^22s-1s^29p$	6.3475	262(47) 289(57)	250(38) 258(60)	254(30) 103(91)	253(30) 145(52)	*N*
Fe XXIV $1s^22s-1s^26p$	6.7870	−413(11) 155(17)	−410(14) 190(18)	−425(11) 145(18)	−426(12) 154(19)	*Y*
Fe XXIV $1s^22s-1s^25p$	7.1690	−409(7) 261(9)	−412(8) 255(9)	−442(8) 244(9)	−452(9) 280(10)	*Y*
Fe XXIV $1s^22s-1s^24p$	7.9893	−344(8) 353(9)	−357(9) 345(10)	−390(9) 319(10)	−405(8) 321(9)	*Y*
Fe XXIV $1s^22s-1s^23p$	10.6190	−385(16) 295(21)	−393(18) 318(23)	−454(18) 286(23)	−454(20) 335(23)	*Y*
Fe XXIV $1s^22s-1s^23p$	10.6630	−358(19) 328(26)	−388(19) 301(23)	−404(19) 317(24)	−386(19) 308(23)	*Y*
Fe XXIII $2s^2-2s5p$	7.4722	−337(16) 243(23)	−351(16) 247(23)	−330(16) 199(22)	−359(16) 105(30)	*Y*
Fe XXIII $2s^2-2s4p$	8.3029	−204(13) 273(15)	−224(14) 291(17)	−296(14) 261(16)	−280(15) 246(16)	*Y*
Fe XXIII $2s^2-2s3p$	10.9810	−379(16) 178(24)	−387(24) 257(33)	−398(17) 176(27)	−390(16) 116(31)	*Y*
Fe XXIII $2s^2-2s3p$	11.0180	−333(18) 150(29)	−315(19) 164(30)	−360(19) 168(30)	−355(19) 189(25)	*Y*
Fe XXII $2s^22p-2s^23d$	11.7700	−307(33) 147(54)	−324(31) 112(67)	−327(29) 95(51)	−372(32) 127(61)	*Y*
Fe XXII $2s^22p-2s^23d$	11.9200	−286(50) 141(80)	−281(62) 173(103)	−358(56) 208(68)	−324(57) 196(81)	*Y*
Mn XXIV $1s^2-1s2p$	2.0062	509(444) 1259(437)	−582(261) 1018(322)	−7(302) 719(572)	−326(184) 294(359)	*Y*
Cr XXIV $1s-2p$	2.0901	−303(156) 644(271)	−262(180) 531(238)	22(176) 404(334)	−331(205) 735(209)	*Y*
Cr XXIII $1s^2-1s2p$	2.1821	−153(169) 852(220)	−476(129) 341(353)	−544(158) 732(225)	−343(127) 497(169)	*Y*
Ca XX $1s-3p$	2.5494	−283(146) 364(183)	−357(214) 442(294)	−296(102) 345(160)	−776(145) 544(182)	*Y*
Ca XX $1s-2p$	3.0203	−414(34) 393(48)	−417(37) 422(45)	−494(34) 388(45)	−436(33) 356(49)	*Y*
Ca XIX $1s^2-1s2p$	3.1772	−391(48) 248(77)	−395(50) 248(88)	−547(58) 198(146)	−427(46) 178(110)	*Y*
Ar XVIII $1s-2p$	3.7329	−431(25) 303(34)	−383(32) 476(47)	−442(31) 335(42)	−468(26) 323(35)	*Y*
S XVI $1s-3p$	3.9912	−420(32) 256(50)	−464(39) 242(58)	−507(37) 197(72)	−433(34) 219(59)	*Y*
S XVI $1s-2p$	4.7292	−421(36) 586(49)	−520(35) 504(46)	−533(25) 347(30)	−355(23) 369(29)	*Y*
S XV $1s2-1s2p$	5.0387	−359(32) 85(66)	−348(41) 132(92)	−415(40) 90(69)	−526(96) 309(143)	*Y*
Si XIV $1s-3p$	5.2172	−360(30) 279(41)	−437(31) 229(45)	−545(34) 294(46)	−470(23) 205(36)	*Y*
Si XIV $1s-2p$	6.1822	−446(10) 311(13)	−464(11) 300(14)	−483(11) 370(14)	−453(10) 303(13)	*Y*
Si XIII $1s^2-1s2p$	6.6480	−343(29) 185(46)	−335(32) 233(40)	−375(25) 171(44)	−373(33) 196(41)	*Y*
Mg XII $1s-7p$	6.4486	−408(27) 139(37)	−395(21) 82(63)	−412(34) 187(46)	−411(28) 176(41)	*Y*
Mg XII $1s-5p$	6.5801	−510(17) 164(28)	−502(16) 146(24)	−510(17) 178(24)	−521(20) 191(31)	*Y*
Mg XII $1s-3p$	7.1062	−365(16) 91(31)	−406(17) 114(25)	−398(20) 114(32)	−381(18) 61(49)	*Y*
Mg XII $1s-2p$	8.4210	−410(9) 339(11)	−427(9) 278(10)	−467(9) 259(10)	−471(10) 263(12)	*Y*
Ne X $1s-4p$	9.7082	−359(25) 151(46)	−390(21) 107(39)	−439(19) 95(30)	−399(21) 141(32)	*Y*
Na XI $1s-2p$	10.0250	−346(19) 166(26)	−339(19) 146(25)	−443(22) 151(27)	−441(20) 127(26)	*Y*
Ne X $1s7p$	9.2912	−418(63) 84(93)	−447(52) 93(84)	−380(74) 199(63)	−391(46) 100(80)	*Y*
Ne X $1s-6p$	9.3616	−776(25) 287(31)	−846(25) 291(32)	−837(34) 250(45)	−945(32) 114(47)	*N*
Ne X $1s-5p$	9.4807	−365(28) 247(32)	−322(28) 194(34)	−370(27) 222(34)	−391(26) 201(33)	*Y*
Ne X $1s-3p$	10.2389	−363(18) 222(25)	−439(20) 229(22)	−407(15) 143(21)	−449(16) 207(20)	*Y*
Ne X $1s-2p$	12.1330	−441(21) 281(25)	−420(21) 225(25)	−452(20) 236(26)	−482(17) 213(27)	*Y*
Ne II	14.6310	−389(34) 182(42)	−393(33) 132(46)	−410(30) 82(73)	−457(46) 223(49)	*Y*
O VIII $1s-4p$	15.1762	−296(90) 361(113)	−329(81) 314(133)	−471(68) 186(101)	−374(42) 41(73)	*Y*
O VIII $1s-3p$	15.9870	−23(63) 151(90)	−9(77) 234(79)	−110(74) 182(111)	−2(80) 200(94)	*N*